Enhancement of aerodynamic performance of a heaving airfoil using synthetic-jet based active flow control

Chenglei Wang & Hui Tang

Department of Mechanical Engineering,

The Hong Kong Polytechnic University, Kowloon, Hong Kong SAR, China

Correspondence to: h.tang@polyu.edu.hk

Abstract

In this study, we explore the use of synthetic jet (SJ) in manipulating the vortices around a rigid heaving airfoil, so as to enhance its aerodynamic performance. The airfoil heaves at two fixed pitching angles, with the Strouhal number, reduced frequency and Reynolds number chosen as St = 0.3, k = 0.25 and Re = 100, respectively, all falling in the ranges for natural flyers. As such, the vortex force plays a dominant role in determining the airfoil's aerodynamic performance. A pair of in-phase SJs is implemented on the airfoil's upper and lower surfaces, operating with the same strength but in opposite directions. Such a fluid-structure interaction problem is numerically solved using a lattice Boltzmann method (LBM) based numerical framework. It is found that, as the airfoil heaves with zero pitching angle, its lift and drag can be improved concurrently when the SJ phase angle ϕ_{sj} relative to the heave motion varies between $\pi/4$ and $3\pi/4$. But this concurrent improvement does not occur as the airfoil heaves with $\pi/6$ pitching angle. Detailed inspection of the vortex evolution and fluid stress over the airfoil surface reveals that, if at good timing, the suction and blowing strokes of the SJ pair can effectively delay or promote the shedding of leading edge vortices, and mitigate or even eliminate the generation of trailing edge vortices, so as to enhance the airfoil's aerodynamic performance. Based on these understandings, an intermittent operation of the SJ pair is then proposed to realize concurrent lift and drag improvement for the heaving airfoil with $\pi/6$ pitching angle.

Keywords: heaving airfoil, synthetic jet, vortex manipulation

1 Introduction

As one of the most sophisticated lift/thrust generation methods found in nature, the flapping motion adopted by birds and insects can provide superior maneuverability and much better aerodynamic performance for low Reynolds number flights [1]. Hence it has been broadly adopted as an effective propulsion method for micro air vehicles (MAVs). For a rigid flapping airfoil, its aerodynamic performance is determined by three types of fluid forces, i.e., the vortex force, added-mass force and viscous force. According to Kang et al. [2], these forces are functions of the Strouhal number (St), reduced frequency (k) and Reynolds number (Re). For natural flyers, St usually falls in the range of 0.2 to 0.4, k is commonly between 0.1 and 0.5, and Re is at least $O(10^1)$ [3]. Under these circumstances, the vortex force plays a dominant role on the airfoil's aerodynamic performance in a great deal of cases in nature. More specifically, in such cases the airfoil's aerodynamic performance mainly depends on its interaction with surrounding vortices, including the leading edge vortex (LEV) and trailing edge vortex (TEV) [1]. Therefore, the flapping airfoil's aerodynamic performance can be greatly improved if the evolution of these vortices are properly manipulated.

Conventional vortex manipulation methods, such as changing airfoil's kinematics, flexibility and morphology, have been widely investigated. Through these methods, a series of lift-enhancement mechanisms has been identified, including the delayed stall [4], rotational circulation [5], wake capture [5], and clap and fling [6, 7]. In addition, drag reduction[8]/thrust enhancement [9] and optimization of propulsive efficiency [10] can also be achieved. On this topic Shyy et al. [1] have given a comprehensive review.

Apart from the aforementioned approaches, vortex manipulation can be realized through a promising active flow control method, i.e., synthetic jet (SJ). An SJ is a chain of vortex rings/pairs produced through a small orifice/slot by the oscillation of single or multiple diaphragms attached to a cavity[11, 12, 13, 14]. An attractive feature of the SJ is that it can produce non-zero momentum flux to influence ambient flows with zero net mass flux. Since emerging, the SJ technology has been extensively applied in plenty of engineering practices, such as the vortex-induced vibration suppression [15, 16], flow separation control [17, 18], and drag reduction [19], just to name a few. The capability of SJ in modifying vortex dynamics in these applications has been well demonstrated. However, the use of this technology on flapping airfoils is rare. Only a few relevant works have been reported. For instance, Mokhtar et al. [20] numerically explored the effects of a synthetic jet on the improvement of aerodynamic perfor-

mance of an airfoil undergoing a figure "8" flapping motion in a uniform flow at a Reynolds number of 10^5 in only one case. No significant enhancement, nevertheless, was observed in their study, and they attributed the reason to the lack of systematic investigations. Çiftci [21] demonstrated that when an airfoil hovers at the Reynolds number of $O(10^3)$, the lift-to-drag ratio could be augmented through implementing a synthetic jet near the leading edge of the airfoil's upper surface.

This study aims to further explore the use of SJ in manipulating the vortices around a rigid heaving airfoil, so as to enhance its aerodynamic performance. Although a three-dimensional wing model is more realistic, two-dimensional investigations can still provide significant insights into the unsteady fluid physics of flapping wings [3]. As such, in this study we adopt an elliptic airfoil heaving with two fixed pitching angles at a Reynolds number 100, where the spanwise flow can be negligible and hence two-dimensional simulations are appropriate [22]. To minimize the influence on the airfoil's aerodynamic forces caused by the SJ's direct momentum injection, a pair of SJs is applied on the airfoil's upper and lower surfaces, operating in phase with the same strength but in opposite directions. For effective and efficient simulations, such a fluid-structure interaction problem is solved using a lattice Boltzmann method (LBM) based numerical framework.

The remaining of this paper is organized as follows: the problem setup and numerical method are described in Section 2, the influence of the SJ pair on the airfoil's aerodynamic performance is presented and discussed in Section 3, in which more flow physics around the airfoil is unveiled through several representative cases, and a conclusion is given in Section 4.

2 Problem description and methodology

2.1 Problem description

In this study, an elliptic airfoil with chord length c and thickness $b = c/4$ is immersed in a uniform flow at a low chord-length-based Reynolds number, i.e., $Re = 100$, as shown in Figure 1. The airfoil oscillates in the cross-flow direction with a fixed pitching angle (θ), and its heaving motion is predefined as

$$h(t) = \frac{h_0}{2}\cos(2\pi f t) \tag{1}$$

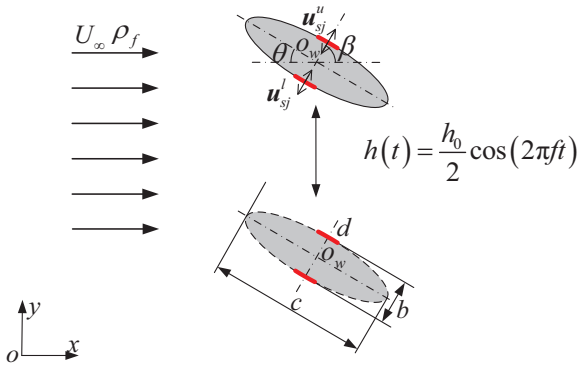

Figure 1: Schematic of a two-dimensional heaving elliptic airfoil equipped with a SJ pair. The two red line sections represent the SJ pair; U_∞ the freestream velocity; ρ_f the fluid density; c the chord length of the airfoil; b the thickness of the airfoil; θ the pitching angle; h_0 the heaving amplitude of the airfoil; f the heaving frequency of the airfoil; $\boldsymbol{u}^u_{sj}$ and $\boldsymbol{u}^l_{sj}$ the velocities of the upper and lower SJs relative to the heaving airfoil, respectively; β the orientation angle of the SJ pair relative to the streamwise direction; and d the SJ width.

where h_0 is the heaving amplitude and f the heaving frequency. Under this circumstance, the Strouhal number (St) and the reduced frequency (k) can be defined, respectively, as

$$St = \frac{fh_0}{U_\infty} \tag{2}$$

$$k = \frac{\pi fc}{U_\infty} \tag{3}$$

where U_∞ is the freestream velocity. In this study, these two parameters are fixed at $St = 0.3$ and $k = 0.25$, both falling in their corresponding ranges selected by natural flyers [3]. Under this condition, the ratio among the fluid force's three major components can be roughly estimated as $vortex\ force : added\ mass\ force : viscous\ force = St^2/k : Stk : St/Rek = 30 : 4.8 : 1$ [2]. As such, in this study the generation and evolution of vortices around the airfoil play a key role in the production of aerodynamic forces, and hence the manipulation of these vortices can significantly change the aerodynamic forces experienced by the airfoil.

To manipulate the vortices generated during both the downstroke and upstroke, a pair of SJs is implemented at the mid chord and on the upper and lower surfaces of the airfoil, respectively, as depicted by the red line sections in Figure 1. In this study, it is assumed that the upper and lower SJs have the same excitation frequency (f_{sj}), phase angle (ϕ_{sj}) and velocity amplitude (U_{sj}), but opposite velocity directions. Hence the forces directly exerted by this SJ pair are substantially cancelled out all the time. In addition, their excitation frequency is set identical to the airfoil's heaving frequency, i.e., $f_{sj} = f$. Under this condition, the time-dependent velocities of the upper and lower SJs ($\boldsymbol{u}^u_{sj}$ and $\boldsymbol{u}^l_{sj}$) relative to the heaving airfoil

can be expressed as

$$\boldsymbol{u}_{sj}^{u} = U_{sj}\cos(2\pi f_{sj}t + \phi_{sj})(\cos\beta, \sin\beta) \tag{4}$$

$$\boldsymbol{u}_{sj}^{l} = -\boldsymbol{u}_{sj}^{u} \tag{5}$$

where β is the orientation angle of the SJ pair relative to the streamwise direction. The SJ velocities are set always perpendicular to the airfoil's chord line, i.e., $\beta + \theta = \pi/2$. A parabolic velocity profile is imposed for each SJ, and thus the momentum coefficient (C_μ) quantifying the SJ strength and power consumption can be written as

$$C_\mu = \frac{8U_{sj}^2 d}{9U_\infty^2 c} \tag{6}$$

where d is the width of each SJ slot, set as 1/10 of the elliptic airfoil's perimeter in this study.

The local fluid stress exerted on the airfoil's surface, $\boldsymbol{\sigma}$, can be evaluated by

$$\boldsymbol{\sigma} = (\sigma_x, \sigma_y) = -(p - p_\infty)\,\boldsymbol{I}\cdot\boldsymbol{n} + \rho_f\nu\,(\nabla\boldsymbol{u} + \boldsymbol{u}\nabla)\cdot\boldsymbol{n} \tag{7}$$

where σ_x and σ_y are the x- and y-component of the fluid stress, respectively, p the local pressure, p_∞ the freestream pressure, $\boldsymbol{I}$ the unit tensor, $\boldsymbol{n}$ the out-normal unit vector to the airfoil's surface, ρ_f the fluid density, ν the fluid kinematic viscosity, ∇ the gradient operator, and $\boldsymbol{u}$ the local velocity vector. Accordingly, the fluid stress coefficient, $\boldsymbol{C_\sigma}$, can be defined as

$$\boldsymbol{C_\sigma} = \left(C_{\boldsymbol{\sigma}_x}, C_{\boldsymbol{\sigma}_y}\right) = \frac{2\boldsymbol{\sigma}}{\rho_f U_\infty^2} \tag{8}$$

where $C_{\boldsymbol{\sigma}_x}$ and $C_{\boldsymbol{\sigma}_y}$ are its x- and y-components, respectively. With them, the lift and drag coefficients can be expressed, respectively, as

$$C_L = \frac{\int_\Omega C_{\boldsymbol{\sigma}_y} d\Omega}{c} \tag{9}$$

$$C_D = \frac{\int_\Omega C_{\boldsymbol{\sigma}_x} d\Omega}{c} \tag{10}$$

where Ω represents the airfoil's surface.

2.2 Methodology

To facilitate this study, the incompressible D2Q9 MRT LBE model [23], i.e., two-dimensional incompressible multiple-relaxation-time lattice Boltzmann equation model with nine discrete velocities, is employed to simulate the two-dimensional flow around the heaving elliptic airfoil. The MRT multi-block scheme proposed by Yu et al. [24] is applied in the present study to

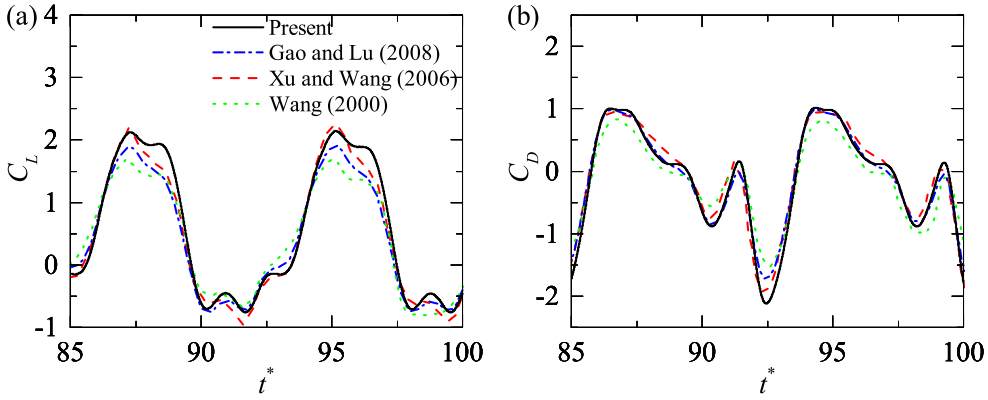

Figure 2: Time histories of the (a) lift and (b) drag coefficients (C_L and C_D) of a hovering elliptic airfoil over two hovering periods at Re = 157.

enhance the computational efficiency while maintaining sound accuracy. Besides, the overlap mesh combined with the interpolated half-way bounce back scheme [25] is incorporated to deal with the moving curved boundaries. More details about the current LBM-based numerical framework and its validation can be found in our previous works [15, 16, 26].

To further validate this framework, a simulation of the flow around an elliptic airfoil hovering in an enclosed domain at Re = 157 is performed, which has been widely investigated by Wang [27], Xu and Wang [28], and Gao and Lu [22] using different numerical methods. In this case, the airfoil heaves and pitches simultaneously, with the heaving amplitude being 2.5 times its chord length and the pitching amplitude equal to $\pi/2$. The phase difference between these two motions is 0. It can be seen from Figure 2 that the results obtained from the current numerical framework agree well with those provided in the literature [22, 27, 28], where the lift and drag coefficients (C_L and C_D) over two hovering periods are compared.

In the present study, the computational domain is set as $60c$(L) × $40c$(W) with a uniform flow moving from the left to the right with a speed U_∞ as depicted in Figure 3. The elliptic airfoil is placed at $20c$ downstream from the inlet boundary. Besides, the entire computational domain is divided into four sets of blocks with the mesh density being increased by a factor of 2 as the block number increases. The block with the finest mesh (i.e., Block 4, mesh spacing Δx) is applied around the airfoil.

The boundary conditions are also shown in Figure 3. At the inlet boundary, the non-reflecting inlet boundary condition proposed by Izquierdo and Fueyo [29] is used, whereas at the outlet boundary the homogenous Neumann boundary condition is implemented. On the top and bottom walls, the Dirichlet boundary condition is applied with the x-component velocity

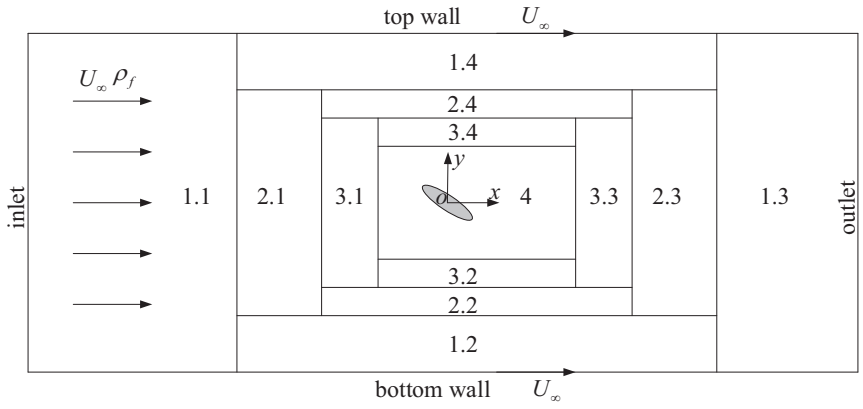

Figure 3: Computational domain with multi-block arrangement (not in scale).

Table 1: Selected cases for the convergence test.

Parameter	Values		
	First case	Second case	Third case
Mesh spacing (Δx)	$c/60$	$c/120$	$c/120$
Freestream velocity (U_∞)	$0.02\Delta x/\Delta t$	$0.02\Delta x/\Delta t$	$0.01\Delta x/\Delta t$
Non-dimensional time step ($U_\infty \Delta t/c$)	1/3000	1/6000	1/12000

U_∞ and y-component velocity 0. The SJ actuators are represented by a number of nodes on the airfoil, and the time-dependent SJ velocities are realized by enforcing $\boldsymbol{u}^u_{sj}$ and $\boldsymbol{u}^l_{sj}$ (Equations 4 and 5) on these nodes. To study the SJ-induced alteration of vortices around the airfoil, the λ_{ci} criteria proposed by Zhou et al. [30] is employed to identify vortices, and isolines of $\lambda_{ci} = 0.2$ are used to represent vortex boundaries.

To ensure the independence of the numerical results on the selected mesh size and time-step, three cases are selected for the convergence study as listed in Table 1, where Δt is the unit time step. In these three cases, the airfoil's pitching angle is set as $\theta = \pi/6$, and the operation parameters for the SJ pair are set as $C_\mu = 0.763$ and $\phi_{sj} = 3\pi/4$. Figure 4 shows that the time histories of the lift and drag coefficients (C_L and C_D) for these three cases are almost indistinguishable, and the differences in their respective time-averaged values are less than 1.2%. Therefore, in order to maintain sound accuracy and save computational efforts, the mesh and time-step settings for the second case, i.e., $\Delta x = c/120$ and $U_\infty \Delta t/c = 1/6000$, are adopted throughout this study.

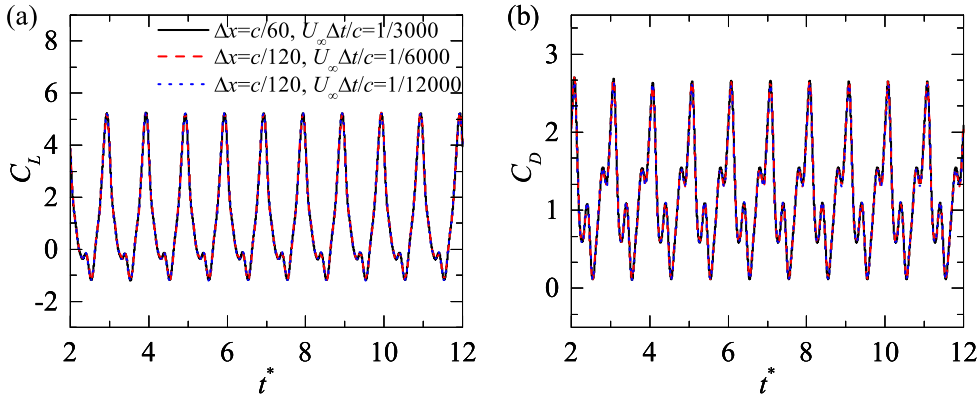

Figure 4: Results for the convergence test: Time histories of the (a) lift and (b) drag coefficients (C_L and C_D) of the heaving elliptic airfoil over ten heaving period when $\theta = \pi/6$, $C_\mu = 0.763$ and $\phi_{sj} = 3\pi/4$. The black solid, red dashed and blue dotted lines correspond to the cases with $\Delta x = c/60$ and $U_\infty \Delta t/c = 1/3000$, $\Delta x = c/120$ and $U_\infty \Delta t/c = 1/6000$, and $\Delta x = c/120$ and $U_\infty \Delta t/c = 1/12000$, respectively.

Table 2: Summary of selected controlled cases.

Parameter	Values
θ	0, $\pi/6$
C_μ	0.048, 0.191, 0.763, 1.716
ϕ_{sj}	0, $\pi/4$, $\pi/2$, $3\pi/4$, π, $5\pi/4$, $3\pi/2$, $7\pi/4$, $2\pi(0)$

2.3 Case summary

According to Section 2.1, in the present study, the capability of the SJ pair in manipulating the vortices around the airfoil and hence the airfoil's aerodynamic performance mainly depends on two key parameters, i.e., the SJ pair's momentum coefficient (C_μ) and phase angle (ϕ_{sj}). The control can also be affected by the the airfoil's pitching angle (θ). Hence, the focus of this study is placed on investigating the effects of the SJ pair operating with various strength and phase angles on the aerodynamic performance of the heaving airfoil that is oriented at different pitching angles. The values for these three parameters are chosen as follows: two θ values are selected, i.e., $\theta = 0$ and $\pi/6$; C_μ varies from 0.048 to 1.716, covering four different values; and eight ϕ_{sj} values are chosen from 0 to 2π with a constant interval $\pi/4$. Therefore, in total 66 cases including two uncontrolled cases are investigated. The controlled cases are summarized and listed in Table 2.

Since the SJ initial forcing condition, i.e., the actuation timing, is important for the control,

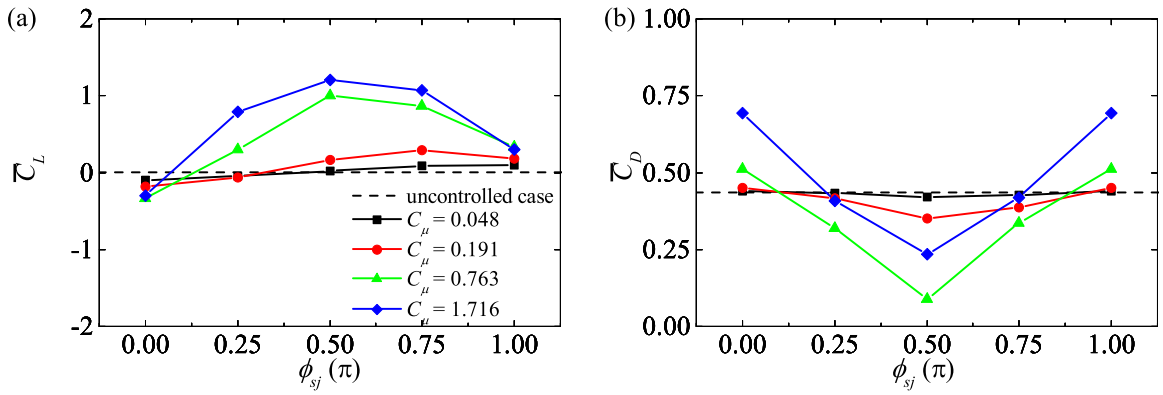

Figure 5: Time-averaged lift and drag coefficients of the heaving elliptic airfoil ($\bar{C}_L$ and $\bar{C}_D$) against the phase angle of the SJ pair (ϕ_{sj}) for the uncontrolled case and the controlled cases with C_μ = 0.048, 0.191, 0.763 and 1.716, when θ = 0.

an investigation has been conducted to study its influence on the resulting flow field before we simulate all planned cases. Although not presented here for the sake of brevity, the comparison revealed that the change of the SJ actuation timing does not affect the steady-state dynamics of the controlled flow. Hence in this study the SJ pair is switched on at the beginning of the downstroke in all cases.

3 Results and Discussions

3.1 Control at θ = 0

Figure 5 provides an overview of the airfoil's time-averaged lift and drag coefficients ($\bar{C}_L$ and $\bar{C}_D$) when the airfoil heaves with zero pitching angle, i.e., θ = 0. For the uncontrolled case, these data are assessed according to the data collected over the periods from the $30th$ to $34th$ heaving cycles. For all the controlled cases, they are evaluated over the periods from the $10th$ to $14th$ heaving cycles after the SJ pair is actuated, within which the transient effects have disappeared. In the uncontrolled case, $\bar{C}_L$ = 0 due to the airfoil's kinematic symmetry, and $\bar{C}_D$ = 0.435, which are represented by the two horizontal dashed lines in Figure 5. Also due to the coincidence of the SJ operating frequency with the airfoil's heaving frequency, in the controlled cases the $\bar{C}_L$ curves are antisymmetric about $\phi_{sj} = 0$ (or π), whereas the $\bar{C}_D$ curves are symmetric. Therefore, only the data in the ϕ_{sj} range from 0 to π are plotted in Figure 5.

Compared to in the uncontrolled case, $\bar{C}_L$ is enhanced and $\bar{C}_D$ is reduced in the majority

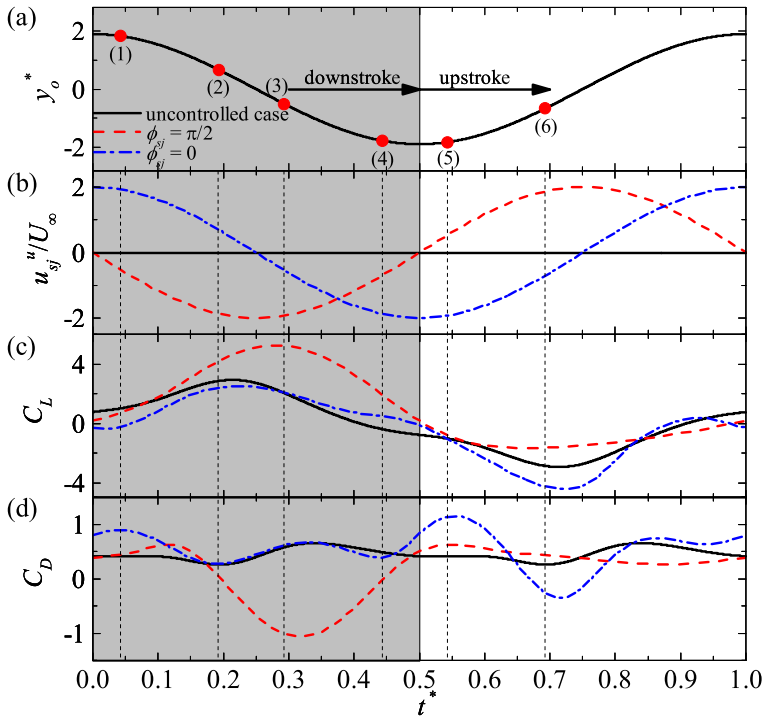

Figure 6: Time histories of the (a) airfoil position (y_o^*), (b) upper SJ velocity (u_{sj}^u), (c) lift, and (d) drag coefficients (C_L and C_D) for the uncontrolled case, the cases with $\phi_{sj} = 0$ and $\pi/2$, when $C_\mu = 0.763$ and $\theta = 0$. The six red dots (•) numbered by (1) to (6) and their corresponding vertical dashed lines represent the six instants, i.e., Instants 1 to 6 respectively corresponding to $t^* = 0.04$, 0.19, 0.29, 0.44, 0.54 and 0.69, at which the vortex pattern and fluid stress coefficient ($\boldsymbol{C_\sigma}$) distribution around the elliptic airfoil's surface for the above three cases are given in Figure 7.

of the controlled cases, as revealed in Figure 5. Specifically, as shown in Figure 5(a), $\bar{C}_L$ is augmented at ϕ_{sj} varying between $\pi/4$ and π, and the maximum value of each $\bar{C}_L$ curve appears at either $\phi_{sj} = \pi/2$ or $\phi_{sj} = 3\pi/4$. This augmentation becomes more obvious as the SJ strength (C_μ) increases. The maximum value among all the controlled cases, $\bar{C}_L = 1.204$, is located at $C_\mu = 1.716$ and $\phi_{sj} = \pi/2$. On the other hand, as shown in Figure 5(b), significant reduction in $\bar{C}_D$ occurs around $\phi_{sj} = \pi/2$. It is interesting to see that the increase of the SJ strength does not result in monotonic $\bar{C}_D$ reduction, which is evidenced by the fact that the SJ pair with a moderate strength, $C_\mu = 0.763$, performs the best in reducing $\bar{C}_D$. The minimum value among all the controlled cases, $\bar{C}_D = 0.089$, is located at $C_\mu = 0.763$ and $\phi_{sj} = \pi/2$, which is a 79.6% reduction from that in the uncontrolled case.

To reveal why the operation of the SJ pair at intermediate phase angles can simultaneously enhance the lift and reduce the drag, six representative cases are selected for further investi-

gations, including the uncontrolled case serving as the baseline case, and five controlled cases, i.e., one case with $\phi_{sj} = 0$ when $C_\mu = 0.763$ as well as four cases with $\phi_{sj} = \pi/2$ when C_μ varies from 0.048 to 1.716. For these cases, the data from the $15th$ heaving cycle after the SJ pair is actuated are used for discussion, and the instant at the beginning of this cycle is defined as $t^* = 0$ for convenience. The same treatments are also applied for all the other cases throughout this study.

In the uncontrolled case, the lift coefficient (C_L) remains positive during almost the entire downstroke (shaded region as shown in Figure 6) with a peak appearing at $t^* = 0.21$, and the C_L variations during the downstroke and upstroke are mirrored about the $C_L = 0$ line, as shown in Figure 6(c). As for the drag coefficient (C_D), it is always positive and repeats twice during one heaving period, with one peak and one trough appearing at $t^* = 0.34$ and 0.19, respectively, during the downstroke, as shown in Figure 6(d).

Since, as revealed in Section 2.1, the vortex force is the dominant fluid force in this study, the variations of C_L and C_D are directly affected by the evolution of the vortices generated from the heaving airfoil, including the leading-edge vortex (LEV) and the trailing-edge vortex (TEV). This can be demonstrated in Figures 7(a) and 7(d), respectively, by the vortex pattern and the fluid stress coefficient ($\boldsymbol{C_\sigma}$) distribution around the airfoil at six selected instants, i.e., Instants 1 to 6 as defined in Figure 6. Note that, for ease of reference, the vortices of interest in Figure 7 are named by the airfoil portion from which they shed and their appearance sequence within one heaving period. For example, $\mathrm{LEV_{U1}}$ refers to the first leading-edge vortex shed from the airfoil's upper surface, and $\mathrm{TEV_{L2}}$ denotes the second trailing-edge vortex shed from the airfoil's lower surface.

During the first half of the downstroke, a leading-edge vortex, i.e., $\mathrm{LEV_{U1}}$, gradually grows and stays close to the airfoil, as evidenced by the vortex patterns at $t^* = 0.04$ (Instant 1) and 0.19 (Instant 2) shown in Figures 7(a1) and 7(a2), respectively. Under this circumstance, the fluid stress on the airfoil's upper surface generally points upwards, and increases with time, as shown in Figures 7(d1) and 7(d2). This is attributed to the fact that a vortex usually corresponds to a low pressure region, and thus can attracts its surrounding flow. Consequently, C_L remains positive during this period, and approaches its maximum at $t^* = 0.21$. As time advances, $\mathrm{LEV_{U1}}$ gradually sheds from the airfoil, as shown in Figures 7(a3) and 7(a4), resulting in reduced upward-oriented or even downward-oriented fluid stress on the airfoil's upper surface, as shown in Figures 7(d3) and 7(d4). As such, C_L decreases and becomes slightly negative at the end of the downstroke.

Besides $\mathrm{LEV_{U1}}$, two trailing-edge vortices, i.e., $\mathrm{TEV_{L1}}$ and $\mathrm{TEV_{L2}}$, form during the first and second halves of the downstroke, respectively, as shown in Figure 7(a). The evolution of these three vortices determines the C_D variation during this period. Specifically, around $t^* = 0.19$ (Instant 2) the strong $\mathrm{LEV_{U1}}$ causes the approximately largest upstream-oriented fluid stress near the leading edge, as shown in Figures 7(a2) and 7(d2). At this instant, $\mathrm{TEV_{L1}}$ has already left the trailing edge, and $\mathrm{TEV_{L2}}$ is still in its infancy, resulting in relatively small downstream oriented fluid stress at the trailing edge. As a consequence, C_D approaches the minimum at $t^* = 0.19$, as shown in Figure 6(d). As time advances, $\mathrm{LEV_{U1}}$ gradually sheds from the leading edge, and $\mathrm{TEV_{L2}}$ becomes mature, as shown in Figure 7(a3). As such, the reduction and augmentation in the fluid stress can be observed at the leading and trailing edges, respectively, as shown in Figure 7(d3). Therefore, C_D approaches its peak around $t^* = 0.34$.

During the upstroke, the above vortex evolution repeats with the signs of vortices reversed and their positions mirrored about the channel centerline, which is evidenced by the mirrored vortex pattern at $t^* = 0.04$ (Instant 1) and 0.54 (Instant 5) as well as at $t^* = 0.19$ (Instant 2) and 0.69 (Instant 6), as shown in Figure 7(a). Under this condition, the fluid stress distribution is also mirrored, as shown in Figure 7(d). Thus, compared to during the downstroke, C_L reverses its sign but holds its magnitude during the upstroke, whereas C_D remains repeated, as indicated in Figure 6.

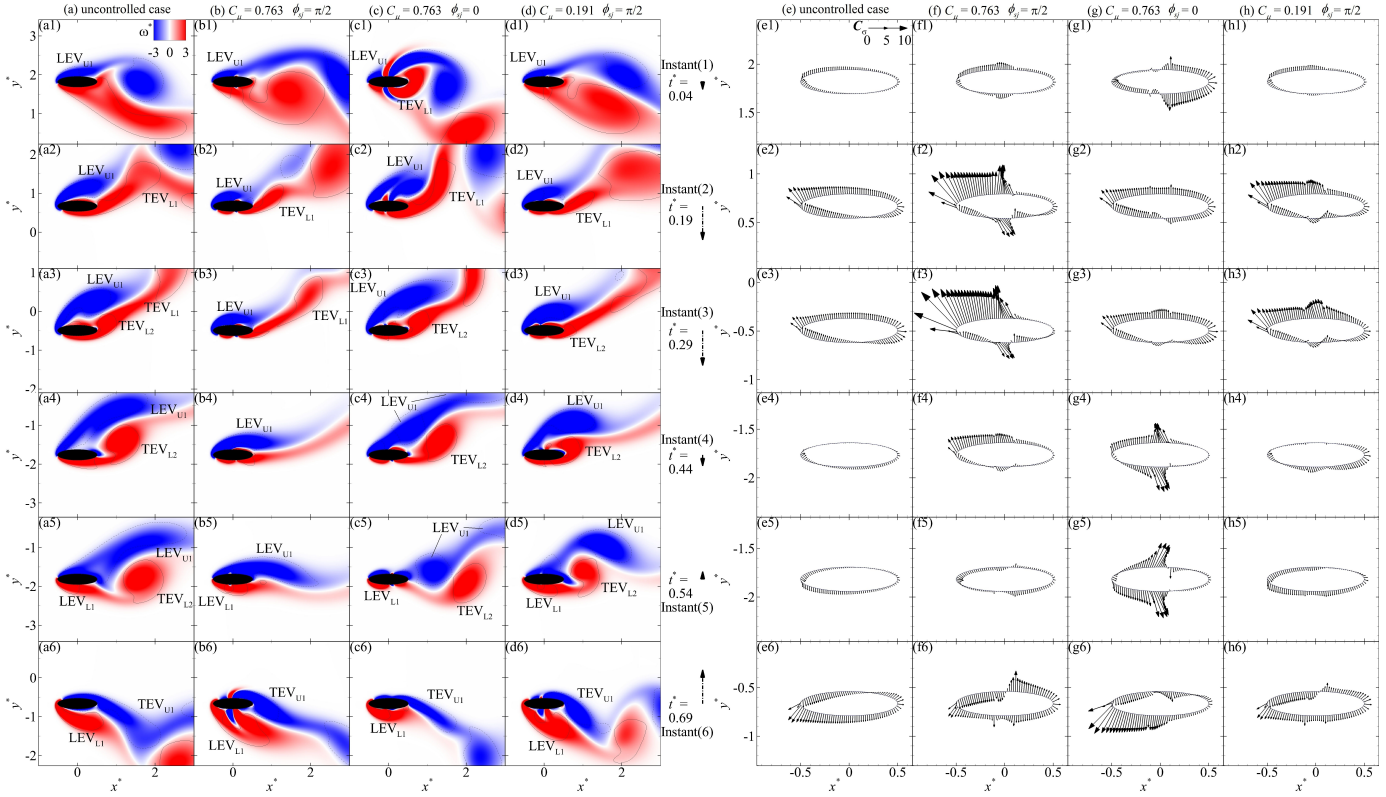

Figure 7: Vortex patterns and $\boldsymbol{C_\sigma}$ distribution around the elliptic airfoil's surface at the six instants, i.e., Instants 1 to 6 indicated in Figure 6 corresponding to the first to the sixth row of this Figure, within one heaving period for the uncontrolled case ((a) and (d)), the case with $\phi_{sj} = \pi/2$ and $C_\mu = 0.763$ ((b) and (e)), and the case with $\phi_{sj} = 0$ and $C_\mu = 0.763$ ((c) and (f)), when $\theta = 0$. The dashed triangle-headed arrow represents the airfoil's moving direction, and its length corresponds to the airfoil's moving speed.

After the SJ pair is switched on, the above C_L and C_D variations change, which can be seen from the two representative cases shown in Figure 6. In the case with $\phi_{sj} = \pi/2$, the SJ pair is in suction during the downstroke, and significant improvements in C_L and C_D can be observed accordingly. Such improvements become the most obvious around the mid downstroke, i.e., $t^* = 0.25$, at which the SJ pair exerts the maximum suction. This is evidenced by the fact that C_L approaches its maximum 5.252 at $t^* = 0.28$, 79.45% larger than that in the uncontrolled case, as shown in Figure 6(c), and C_D reaches its minimum −1.062 at $t^* = 0.32$, meaning that thrust is produced around this instant, as shown in Figure 6(d).

The above observation implies a positive correlation between the improvement of the airfoil's aerodynamic performance and the suction of the SJ pair. Unlike in the uncontrolled case where $\mathrm{LEV_{U1}}$ starts to shed around $t^* = 0.25$, $\mathrm{LEV_{U1}}$ remains attached to the airfoil's upper surface during the entire downstroke due to the suction of the upper SJ, as evidenced by the vortex pattern shown in Figures 7(b1) to 7(b4). Hence, the fluid stress between the leading edge and the upper SJ slot remains upward-oriented and is evidently augmented during this period, as shown in Figures 7(e1) to 7(e4). Meanwhile, the upstream-oriented fluid stress near the leading edge is also greatly enhanced. On the other hand, the TEV evolution is also modified by the suction of the SJ pair, compared to in the uncontrolled case. That is, only one TEV, i.e., $\mathrm{TEV_{L1}}$, is produced during the downstroke, whereas $\mathrm{TEV_{L2}}$ does not appear, as shown in Figures 7(b1) to 7(b4). The prevention of $\mathrm{TEV_{L2}}$ production relieves the downstream-oriented fluid stress near the trailing edge during the second half of the downstroke, as evidenced by the vortex pattern and fluid stress distribution at $t^* = 0.29$ (Instant 3), as shown in Figures 7(b3) and 7(e3), respectively. As a consequence, C_L and C_D are both improved.

Additionally, a moderate C_L enhancement is found approximately at $t^* = 0.69$ (Instant 6) during the upstroke, as shown in Figure 6(c). Around this instant, $\mathrm{LEV_{L1}}$ evolves under the airfoil's lower surface, but it goes farther from the airfoil than that in the uncontrolled case due to the strong blowing of the lower SJ, as shown in Figures 7(a6) and 7(b6). Under this circumstance, the downward-oriented fluid stress between the leading edge and the lower SJ slot is weakened, as shown in Figure 7(e6). Furthermore, the boundary layer on the airfoil's upper surface is cut into two pieces by the upper SJ vortex pair, whose downstream branch strengthens $\mathrm{TEV_{U1}}$, compared to in the uncontrolled case, as shown in Figures 7(a6) and 7(b6). This results in slight augmentation of downward-oriented fluid stress between the leading edge and the upper SJ slot, and significant augmentation of upwards-oriented fluid stress between the upper SJ slot and the trailing edge, as shown in Figure 7(e6). Thus, C_L is enhanced at this

instant.

In contrast to the case with $\phi_{sj} = \pi/2$, no significant improvement in C_L or C_D is observed over the entire heaving period in the case with $\phi_{sj} = 0$, as shown in Figures 6(c) and 6(d). What is worse, degraded aerodynamic performance is seen at some instants compared to in the uncontrolled case, i.e., the reduction in C_L around $t^* = 0.04$ (Instant 1) and 0.69 (Instant 6), and the augmentation in C_D right after the stroke reversals, i.e., at $t^* = 0.04$ (Instant 1) and 0.54 (Instant 5). Eventually, $\bar{C}_L$ decreases to -0.334 and $\bar{C}_D$ increases to 0.513 (augmented by 18%), as indicated in Figure 5. The reasons for these degradations at the corresponding instants are interpreted as follows.

At the beginning of downstroke, i.e., around $t^* = 0.04$, the SJ pair is around its maximum blowing, as shown in Figure 6(b). Under this condition, $\mathrm{LEV_{U1}}$ is slightly weakened by the upstream branch of the upper SJ vortex pair, as shown in Figure 7(c1). Meanwhile, $\mathrm{TEV_{L1}}$ is obviously strengthened by the downstream branch of the lower SJ vortex pair, and it wraps around the trailing edge. Thus, significant modifications in the fluid stress can be observed on the downstream portion of the airfoil's surface covered by $\mathrm{TEV_{L1}}$, as shown in Figure 7(f1). In this region, all the out-normal fluid stress increases compared to in the uncontrolled case, and such an increase is more significant on the airfoil's lower surface, as shown in Figures 7(d1) and 7(f1). These modifications are mainly responsible for the decrease in C_L and the increase in C_D at this instant.

As the airfoil starts its upstroke at $t^* = 0.54$ (Instant 5), the SJ pair is around its maximum suction, as shown in Figure 6(b). Under this condition, all the nearby vortices are attracted to the airfoil's surface, as shown in Figure 7(c5). The fluid stress on the upstream portion of the airfoil's surface becomes inclined towards the freestream direction and increases evidently, as shown in Figures 7(d5) and 7(f5). As such, C_D is augmented around this instant. As time advances to $t^* = 0.69$ (Instant 6), $\mathrm{LEV_{L1}}$ stays closer to the airfoil's lower surface than in the uncontrolled case due to the suction of the lower SJ, as shown in Figures 7(a6) and 7(c6). This greatly enhances the downwards-oriented fluid stress between the leading edge and the lower SJ slot as well as the upstream-oriented fluid stress around the leading edge, as plotted in Figure 7(f6). As a consequences, the lift and drag are concurrently reduced at this instant.

By comparing the above two representative cases, it is found that when ϕ_{sj} is shifted from $\pi/2$ to 0, the SJ pair loses its capability in enhancing the airfoil's aerodynamic performance. This stems from the fact that, in the $\phi_{sj} = 0$ case where the suction stroke starts at $t^* = 0.25$,

the SJ pair misses the best timing for attracting $\mathrm{LEV_{U1}}$, whose initial development is in the first half of the downstroke, i.e., $t^* < 0.25$. This is well evidenced by the vortex pattern in this case at $t^* = 0.29$ (Instant 3) and 0.44 (Instant 4) shown in Figures 7(c3) and 7(c4). As such, no apparent modification on the fluid stress is achieved, as shown in Figures 7(f3) and 7(f4). This implies that the phase angle determines the timing of interactions between the SJ pair and LEVs/TEVs, thus the extent of modifications in the fluid stress, and then the resultant lift and drag experienced by the airfoil. Therefore, in order to improve the airfoil's aerodynamic performance, ϕ_{sj} should be appropriately selected.

Besides the phase angle, the strength of the SJ pair also affects the airfoil's aerodynamic performance, as revealed in Figure 5. That is, in general the stronger the SJ pair is, the greater improvement the airfoil can achieve. This observation can be further confirmed through comparing the C_L and C_D time histories in the cases with C_μ varying from 0.048 to 1.716 when $\phi_{sj} = \pi/2$, as shown in Figure 8. In all these cases the SJ pair is able to increase C_L during the downstroke and reduce C_D around the mid downstroke, i.e., $t^* = 0.25$. The improvement becomes more evident as C_μ increases. The reason is obvious: the stronger SJ pair is more capable of altering the nearby vortices and hence the resulting fluid stress over the airfoil. However, our results also indicate that a larger C_μ does not always guarantee better aerodynamic performance. For example, with ϕ_{sj} fixed at $\pi/2$, $\bar{C}_D$ approaches its minimum at $C_\mu = 0.763$ rather than 1.716, as revealed in Figure 5. The C_D time histories reveal that, in the case with $C_\mu = 1.716$, C_D is pronouncedly larger than that in the case with $C_\mu = 0.763$ around $t^* = 0.04$ (Instant 1) and 0.69 (Instant 6), as shown in Figure 8(b). Although not shown here for brevity, this results from the fact that, as C_μ increases from 0.763 to 1.716, the fluid stress which is inclined slightly downstream around the SJ slots becomes larger approximately at $t^* = 0.04$, and the downstream-oriented fluid stress around the trailing edge increases due to the strengthened $\mathrm{TEV_{U1}}$ around $t^* = 0.69$. Therefore, in order to improve the aerodynamic performance of the heaving airfoil, a proper, instead of a larger, C_μ is desired.

3.2 Control at $\theta = \pi/6$

The preceding section reveals that the SJ pair is able to greatly improve the aerodynamic performance of the airfoil when its pitching angle (θ) is fixed at 0. In engineering practice, however, heaving airfoils with non-zero pitching angles are more common. Therefore, this section is devoted to investigating the capability of the SJ pair in enhancing the aerodynamic

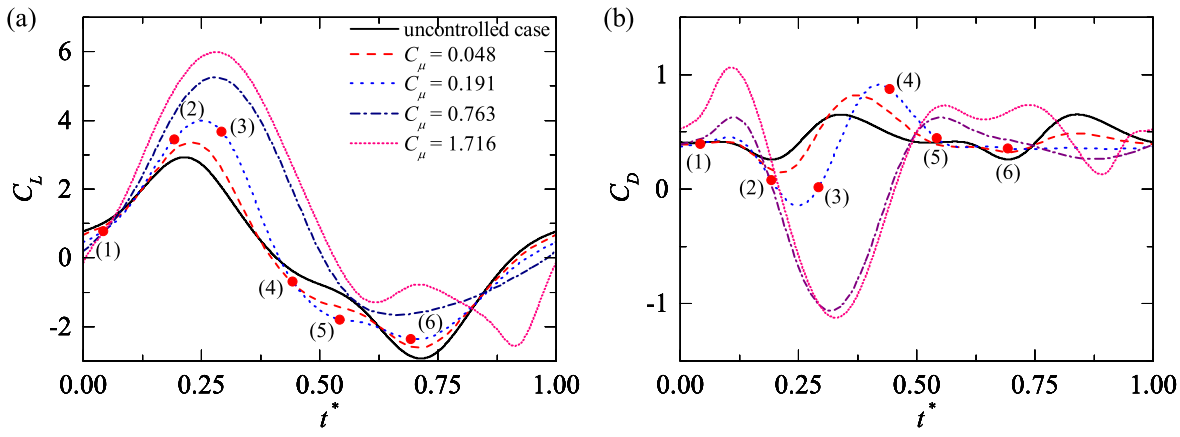

Figure 8: Time histories of the (a) lift and (b) drag coefficients (C_L and C_D) of the heaving airfoil with $\theta = 0$ for the uncontrolled case and the cases with different C_μ, when $\phi_{sj} = \pi/2$. The six red dots (•) numbered by (1) to (6) represent the six instants, i.e., Instants 1 to 6 respectively corresponding to $t^* = 0.04$, 0.19, 0.29, 0.44, 0.54 and 0.69, at which the vortex pattern and fluid stress coefficient ($\boldsymbol{C_\sigma}$) distribution around the elliptic airfoil's surface for the cases with $C_\mu = 0.191$ and 0.763 are given in Figure 7.

performance of the airfoil with a non-zero pitching angle, i.e., $\theta = \pi/6$.

Figure 9 provides an overview of the non-zero pitching airfoil's time-averaged lift and drag coefficients ($\bar{C}_L$ and $\bar{C}_D$). In the uncontrolled case $\bar{C}_L = 0.863$ and $\bar{C}_D = 0.969$, as denoted by the two horizontal dashed lines in Figure 9, respectively. As expected, these two values are larger than those in the uncontrolled, zero pitching case due to the increased angle of attack.

After the SJ pair is switched on, it is seen from Figure 9(a) that $\bar{C}_L$ is enhanced when the phase angle (ϕ_{sj}) falls into the range of $\pi/2$ to π, outside which it is significantly reduced. Within this ϕ_{sj} range, more effective increase in $\bar{C}_L$ can be achieved as the strength of the SJ pair (C_μ) increases. Particularly, when $C_\mu \leq 0.191$, the increase in $\bar{C}_L$ is very limited and the maximum enhancement is achieved at $\phi_{sj} = \pi$; as C_μ becomes larger, significant enhancement of $\bar{C}_L$ can be obtained at $\phi_{sj} = 3\pi/4$. Among all the controlled cases, the maximum $\bar{C}_L = 1.493$ is achieved in the case with $C_\mu = 1.716$ and $\phi_{sj} = 3\pi/4$, which is 73% larger than that in the uncontrolled case.

As for $\bar{C}_D$, it is slightly reduced in the ϕ_{sj} range of $3\pi/2$ to 2π, whereas it is significantly increased outside this range, as shown in Figure 9(b). When $\phi_{sj} = 7\pi/4$ and the SJ strength is moderate, i.e., $C_\mu = 0.763$, the largest reduction in $\bar{C}_D$ is achieved. Under this condition, $\bar{C}_D = 0.813$ is reduced by 16.1% compared to that in the uncontrolled case. This, again, confirms that the stronger SJ pair is not always more beneficial in reducing the drag.

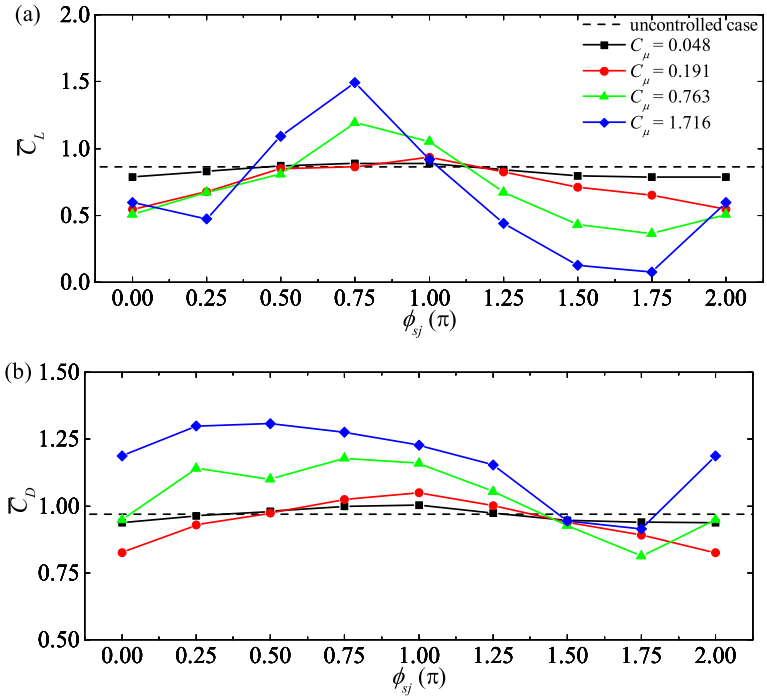

Figure 9: Time-averaged lift and drag coefficients of the heaving elliptic airfoil ($\bar{C}_L$ and $\bar{C}_D$) against the phase angle of the SJ pair (ϕ_{sj}) for the uncontrolled case and the controlled cases with C_μ = 0.048, 0.191, 0.763 and 1.716, when $\theta = \pi/6$.

From Figures 9(a) and 9(b), it is found that the ϕ_{sj} ranges for increasing $\bar{C}_L$ and for reducing $\bar{C}_D$ are not overlapped. This means that, unlike for the zero pitching airfoil, it is impossible to simultaneously improve $\bar{C}_L$ and $\bar{C}_D$ using the same SJ operation when the airfoil heaves with $\pi/6$ pitching angle.

To reveal the reasons and also to seek a way to overcome this limitation, three representative cases are selected for further investigations, including the uncontrolled case and two controlled cases with C_μ = 0.763, i.e., one case with $\phi_{sj} = 3\pi/4$ where $\bar{C}_L$ and $\bar{C}_D$ are simultaneously increased by 38.2% and 21.7%, respectively, and the other case with $\phi_{sj} = 7\pi/4$ where $\bar{C}_L$ and $\bar{C}_D$ are simultaneously reduced by 58.1% and 16.1%, respectively.

Since the non-zero pitching angle breaks the airfoil's kinematic symmetry, in the uncontrolled case the lift coefficient (C_L) during the downstroke and upstroke is no longer mirrored about the $C_L = 0$ line, and the drag coefficient (C_D) no longer repeats in the two strokes, as shown in Figure 10. The $\pi/6$ pitching angle also introduces positive effective angles of attack to the airfoil in most of the time. Hence, C_L remains large positive over most of the heaving period, approaching its positive maximum $C_L = 2.921$ at $t^* = 0.18$, and it becomes negative only around the mid upstroke, approaching its negative maximum $C_L = -1.233$ at $t^* = 0.74$, as

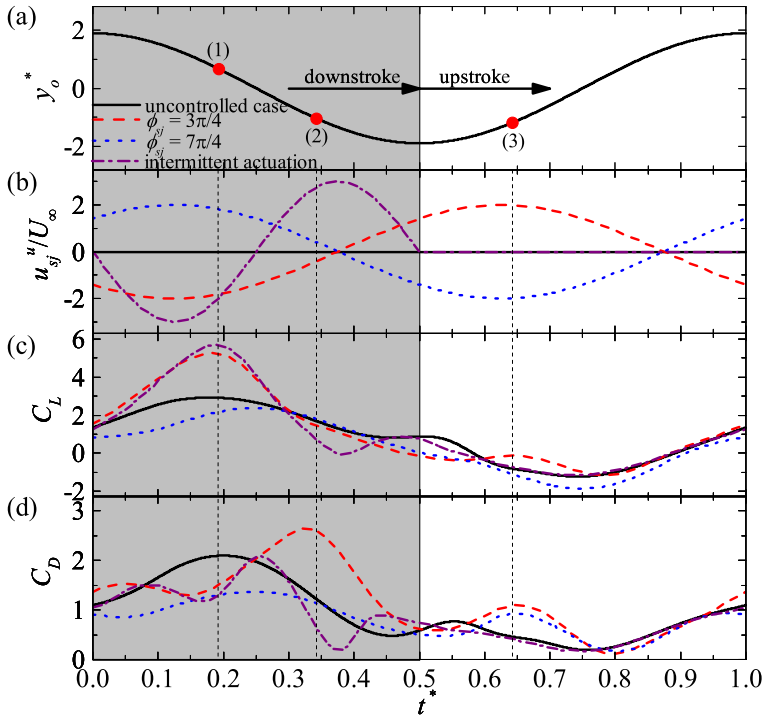

Figure 10: Time histories of the (a) airfoil position (y_o^*), (b) upper SJ velocity (u_{sj}^u), (c) lift, and (d) drag coefficients (C_L and C_D) for the uncontrolled case, the case with $\phi_{sj} = 3\pi/4$ and $C_\mu = 0.763$, the case with $\phi_{sj} = 7\pi/4$ and $C_\mu = 0.763$, and the intermittent-actuation controlled case, when $\theta = \pi/6$. The three red dots (•) numbered by (1) to (3) and their corresponding vertical dashed lines represent the three instants, i.e., Instants 1 to 3 respectively corresponding to $t^* = 0.19$, 0.34 and 0.64, at which vortex pattern and fluid stress coefficient ($\boldsymbol{C_\sigma}$) distribution around the elliptic airfoil's surface for the above four cases are given in Figure 11.

shown in Figure 10(c). As for C_D, it remains positive during the entire heaving period, and exhibits a variation trend similar to that of C_L, with its maximum C_D = 2.097 appearing at t^* = 0.2 and its minimum C_D = 0.19 appearing at t^* = 0.76, as shown in Figure 10(d).

The C_L and C_D variations are closely related to the generation and evolution of LEVs and TEVs. During the first half of the downstroke, $\mathrm{LEV_{U1}}$ and $\mathrm{TEV_{L1}}$ form and then start to leave the airfoil's upper surface at around t^* = 0.19 (Instant 1), as shown in Figure 11(a1). Under this condition, the fluid stress over the airfoil's upper surface approaches the largest around this instant, as shown in Figure 11(e1), resulting in the maximum C_L and C_D at t^* = 0.18 and 0.2, respectively, as shown in Figure 10. During the second half of the downstroke, $\mathrm{LEV_{U1}}$ and $\mathrm{TEV_{L1}}$ gradually shed from the airfoil, causing the continuous reduction in the fluid stress over the airfoil's upper surface. This can be evidenced by comparing the vortex pattern and the fluid stress distribution at t^* = 0.19 (Instant 1) and 0.34 (Instant 2), as shown in Figure 11. Accordingly, C_L and C_D gradually diminish during this period. In the course of the upstroke, no LEV or TEV is produced, as demonstrated by the vortex pattern at t^* = 0.64 (Instant 3) shown in Figure 11(a3). As such, the fluid stress and the resultant lift and drag during this period are generally less significant than during the downstroke, as indicated in Figure 10.

In the controlled case with $\phi_{sj} = 3\pi/4$, a large increase in C_L is observed at around t^* = 0.19 (Instant 1), whereas C_L remains close to that in the uncontrolled case at other instants, as shown in Figure 10(c). In addition, C_D reduces also at around t^* = 0.19, while it is augmented at around t^* = 0.64 (Instant 3) and more significantly at around t^* = 0.34 (Instant 2), as shown in Figure 10(d). The reasons for these changes can be clearly seen from the vortex pattern and fluid stress distribution at the corresponding instants, as shown in Figure 11. At t^* = 0.19, the SJ pair exerts strong suction, delaying the shedding of $\mathrm{LEV_{U1}}$ from the airfoil's upper surface as shown in Figure 11(b1). Under this condition, the upstream-oriented fluid stress near the leading edge becomes larger than in the uncontrolled case, so does the upward-oriented fluid stress between the leading edge and the upper SJ slot, as shown in Figure 11(f1). Meanwhile, $\mathrm{TEV_{L1}}$ has already shed, and a small new $\mathrm{TEV_{L2}}$ appears near the trailing edge, leading to a slight reduction in the fluid stress in this region. As such, C_L and C_D are improved simultaneously at around this instant. Approximately at t^* = 0.34, the suction strength of the SJ pair becomes marginal, and thus $\mathrm{LEV_{U1}}$ left the airfoil's upper surface, as shown in Figure 11(b2). Meanwhile, $\mathrm{TEV_{L2}}$ grows and stays close to the trailing edge, resulting in larger downstream-oriented fluid stress around the trailing edge compared to that in the uncontrolled case, as shown in Figures 11(e2) and 11(f2). Hence C_D is augmented at this instant. As time

advances to $t^* = 0.64$, a new $\mathrm{TEV_{U1}}$ has emerged and is strengthened by the downstream branch of the upper SJ vortex pair, as shown in Figure 11(b3). As such, the downstream-oriented fluid stress between the upper SJ slot and the trailing edge becomes larger than in the uncontrolled case, as shown in Figures 11(e3) and 11(f3), which is mainly responsible for the C_D increase at this instant.

By comparing the above case with a representative case in Section 3.1, i.e., the case with $C_\mu = 0.763$ and $\phi_{sj} = \pi/2$ when the airfoil heaves with zero pitching angle, it reveals that in these two cases the instantaneous C_L and C_D can be concurrently improved during the downstroke through attracting $\mathrm{LEV_{U1}}$ to the airfoil's upper surface. It is interesting to see that both these two cases have their respective maximum $\bar{C}_L$ at $C_\mu = 0.763$, as plotted in Figures 5 and 9, but at different phase angles (one is $\phi_{sj} = 3\pi/4$ and the other is $\phi_{sj} = \pi/2$). This difference stems from the fact that $\mathrm{LEV_{U1}}$ becomes stronger and evolves faster as the pitching angle increases, as demonstrated in Figures 7(a2) and 11(a1), and hence the SJ pair is required to start its suction stroke earlier to exert effective vortex attraction.

In the case with $\phi_{sj} = 7\pi/4$, the most obvious changes in C_L and C_D are observed at around $t^* = 0.19$ (Instant 1), where C_L and C_D are both greatly reduced, as shown in Figure 10. At this instant, the SJ pair is right after its maximum blowing. Hence $\mathrm{LEV_{U1}}$ is cut into two pieces, and $\mathrm{TEV_{L1}}$ is forced to move farther away from the trailing edge, as shown in Figure 11(c1). However, the manipulation of $\mathrm{LEV_{U1}}$ and $\mathrm{TEV_{L1}}$ does not evidently alter the fluid stress on the airfoil's upper surface, as shown in Figure 11(g1), probably due to the involvement of the upper SJ vortex pair. On the other hand, the blowing of the lower SJ offsets the incoming flow and creates a relatively lower-pressure region along the lower surface from the lower SJ slot to the trailing edge. This reverses the direction of the fluid stress in this region compared to in the uncontrolled case, as shown Figures 11(e1) and 11(g1). Consequently, C_L and C_D are mitigated around this instant.

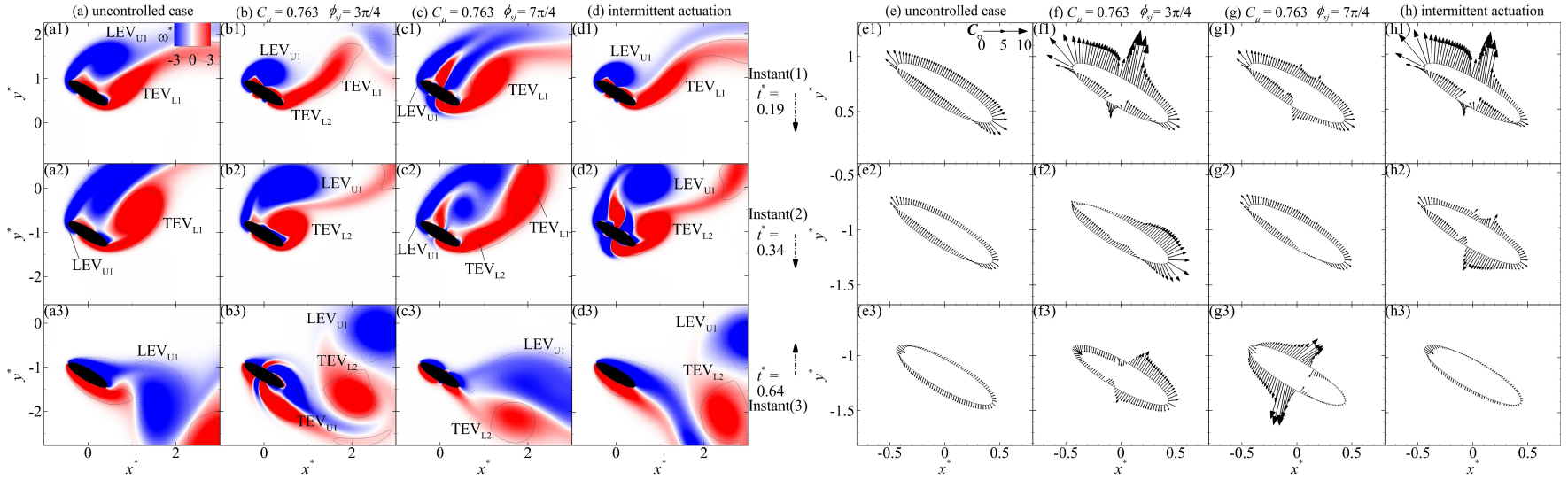

Figure 11: Vortex patterns and $\boldsymbol{C_\sigma}$ distribution around the elliptic airfoil's surface at the three instants, i.e., Instants 1 to 3 indicated in Figure 10 corresponding to the first to the third row of this Figure, within one heaving period for the uncontrolled case ((a) and (e)), the case with $\phi_{sj} = 3\pi/4$ and $C_\mu = 0.763$ ((b) and (f)), the case with $\phi_{sj} = 7\pi/4$ and $C_\mu = 0.763$ ((c) and (g)), and the intermittent-actuation controlled case ((c) and (g)), when $\theta = \pi/6$. The dashed triangle-headed arrow represents the airfoil's moving direction, and its length corresponds to the airfoil's moving speed.

The above two controlled cases reveal that when $\theta = \pi/6$ the delayed $\mathrm{LEV_{U1}}$ shedding can help enhance the lift and reduce the drag, while the appearance of $\mathrm{TEV_{L2}}$ and $\mathrm{TEV_{U1}}$ near the trailing edge is mainly responsible for the drag augmentation. Therefore, if the SJ pair can attract $\mathrm{LEV_{U1}}$ to the airfoil and promptly repel or even eliminate $\mathrm{TEV_{L2}}$ and $\mathrm{TEV_{U1}}$, simultaneous lift and drag improvement can be realized. To prove this conjecture, a SJ pair operating with $C_\mu = 1.716$ and an excitation frequency twice the heaving frequency (i.e., $f_{sj} = 2f$) is adopted for demonstration. In this case, the SJ pair starts its suction at the beginning of the airfoil's downstroke and only operates during the downstroke, as depicted in Figure 10(b). The simulation results show that this intermittently-actuated SJ pair greatly enhances C_L and reduce C_D at around $t^* = 0.19$ (Instant 1) by delaying the shedding of $\mathrm{LEV_{U1}}$, as demonstrated by Figures 10 and 11. Additionally, C_D can also be mitigated at around $t^* = 0.34$ (Instant 2) through fast repelling $\mathrm{TEV_{L2}}$ from the trailing edge and benefiting from the appearance of the downstream branch of the lower SJ vortex pair, as shown in Figures 11(b2) and 11(d2). During the upstroke, the SJ pair is turned off. Thus, $\mathrm{TEV_{U1}}$ is not provoked, and the wake pattern and the fluid stress distribution appear similar to those in the uncontrolled case, as shown in Figure 11. As such, the variations of C_L and C_D in this case are similar to those in the uncontrolled case during this period, as shown in Figure 10. Under this circumstance, $\bar{C}_L$ is increased by 31.89% and simultaneously $\bar{C}_D$ is reduced by 12.36%.

4 Conclusion

We study the capability of an in-phase SJ pair in improving the aerodynamic performance of an elliptic airfoil heaving with two fixed pitching angles, i.e., $\theta = 0$ and $\pi/6$, at the Strouhal number 0.3, reduced frequency 0.25 and Reynolds number 100. The SJ pair operates with the same frequency with the airfoil's heaving motion. The focus is then placed on the influences of the SJ pair's operating phase angle (ϕ_{sj}) and strength (C_μ) on the airfoil's LEVs and TEVs and resultant aerodynamic forces. The major findings are as follows:

1. When the airfoil heaves with zero pitching angle, i.e., $\theta = 0$, the LEV generated during the downstroke makes positive contributions to the lift production, whereas the LEV generated during the upstroke makes negative contributions. On the other hand, LEVs are always beneficial to drag reduction, while TEVs do the opposite. These observations suggest that an effective way of enhancing the lift is to delay the shedding of LEVs during

the downstroke, and to promote fast shedding of LEVs or suppress LEV formation during the upstroke. Additionally, to reduce the drag, it is suggested to postpone the shedding of LEVs over the entire heaving stroke, and to promote fast shedding of TEVs or to suppress TEV formation.

2. When the SJ pair is applied, the zero-pitching airfoil's lift and drag can be improved concurrently at ϕ_{sj} varying roughly from $\pi/4$ to $3\pi/4$, and such an improvement is the most significant when $\phi_{sj} = \pi/2$. This is because that, at this phase angle, the SJ pair can effectively delay the shedding of $\mathrm{LEV_{U1}}$ during the downstroke, promote fast shedding of $\mathrm{LEV_{L1}}$ during the upstroke, and mitigate or even eliminate $\mathrm{TEV_{L2}}$. As ϕ_{sj} deviates from $\pi/2$, the SJ pair gradually misses the best timing for the aforementioned vortex manipulation, and thus becomes less effective.

3. When the airfoil heaves with non-zero pitching angle, i.e., $\theta = \pi/6$, the concurrent lift and drag improvement cannot be achieved by applying the SJ pair of the same settings. The SJ pair can only improve one of them even though ϕ_{sj} is carefully selected. Specifically, the lift can be enhanced only when ϕ_{sj} is around $3\pi/4$, whereas the drag can be reduced only when ϕ_{sj} is around $7\pi/4$. An intermittent operation of the SJ pair is then proposed to realize concurrent lift and drag improvement through attracting $\mathrm{LEV_{U1}}$ to the airfoil, promptly repelling $\mathrm{TEV_{L2}}$, and suppressing $\mathrm{TEV_{U1}}$ formation.

4. Although more effective on vortex manipulation, more SJ strength may not always result in more drag reduction. Therefore, a SJ pair with proper, rather than larger, strength is preferred for drag reduction.

We notice that, to enable effective control, the SJ pair is quite strong compared to the freestream, which may not be appropriate from the practical point of view. The surprisingly strong SJ seems unavoidable in the current low Reynolds number flow where higher jet momentum is usually required to overcome the viscosity effect [15]. Nevertheless, this preliminary study still confirms the capacity of the SJ pair in improving the aerodynamic performance of flapping airfoils. In the near future, we will continue investigating the effects of Reynolds number, Strouhal number and reduced frequency, and other SJ parameters, such as the SJ location, orientation and frequency, on the control.

Acknowledgement

We gratefully acknowledge the financial support for this study from the Research Grants Council of Hong Kong under General Research Fund (Project No. PolyU 152493/16E) and the Departmental General Research Fund (Project No. G-UA5A & G-YBLP) from the Department of Mechanical Engineering of The Hong Kong Polytechnic University. We also acknowledge Dr Zheng Fan from School of Mechanical and Aerospace Engineering, Nanyang Technological University, for covering some of the computational costs for this study.

References

[1] W. Shyy, H. Aono, C.K. Kang, and H. Liu. *An introduction to flapping wing aerodynamics*, volume 37. Cambridge University Press, 2013.

[2] C.K. Kang, H. Aono, C. E. S. Cesnik, and W. Shyy. Effects of flexibility on the aerodynamic performance of flapping wings. *J. Fluid Mech.*, 689:3274, 2011.

[3] W. Shyy, Y.S. Lian, J. Tang, D. Viieru, and H. Liu. *Aerodynamics of low Reynolds number flyers*, volume 22. Cambridge University Press, 2007.

[4] C.P. Ellington, C. Van Den Berg, A.P. Willmott, and A.L.R Thomas. Leading-edge vortices in insect flight. *Nature*, 384(6610):626, 1996.

[5] M.H. Dickinson, F.O. Lehmann, and S.P. Sane. Wing rotation and the aerodynamic basis of insect flight. *Science*, 284(5422):1954–1960, 1999.

[6] T. Weis-Fogh. Quick estimates of flight fitness in hovering animals, including novel mechanisms for lift production. *J. Exp. Biol.*, 59(1):169–230, 1973.

[7] G.R. Spedding and T. Maxworthy. The generation of circulation and lift in a rigid two-dimensional fling. *J. Fluid Mech.*, 165:247–272, 1986.

[8] D.K. Kim, J.H. Han, and K.J. Kwon. Wind tunnel tests for a flapping wing model with a changeable camber using macro-fiber composite actuators. *Smart Mater. Struct.*, 18(2): 024008, 2009.

[9] K.B. Lua, S.M. Dash, T.T. Lim, and K.S. Yeo. On the thrust performance of a flapping two-dimensional elliptic airfoil in a forward flight. *J. Fluids Struct.*, 66:91–109, 2016.

[10] S. Ramananarivo, R. Godoy-Diana, and B. Thiria. Rather than resonance, flapping wing flyers may play on aerodynamics to improve performance. *Proc Natl Acad Sci U S A*, 108 (15):5964–5969, 2011.

[11] B. L. Smith and A. Glezer. The formation and evolution of synthetic jets. *Phys. Fluids*, 10(9):2281–2297, 1998.

[12] A. Glezer and M. Amitay. Synthetic jets. *Annu. Rev. Fluid Mech.*, 34(1):503–529, 2002.

[13] S. Zhong, M. Jabbal, H. Tang, L. Garcillan, F. Guo, N. Wood, and C. Warsop. Towards the design of synthetic-jet actuators for full-scale flight conditions. *Flow Turbul. Combust*, 78(3-4):283–307, 2007.

[14] H. Tang, S. Zhong, M. Jabbal, L. Garcillan, F. Guo, N. Wood, and C. Warsop. Towards the design of synthetic-jet actuators for full-scale flight conditions. *Flow Turbul. Combust*, 78(3-4):309–329, 2007.

[15] C. Wang, H. Tang, F. Duan, and S.C.M. Yu. Control of wakes and vortex-induced vibrations of a single circular cylinder using synthetic jets. *J. Fluids Struct.*, 60:160–179, 2016.

[16] C. Wang, H. Tang, S.C.M. Yu, and F. Duan. Control of vortex-induced vibration using a pair of synthetic jets: Influence of active lock-on. *Phys. Fluids*, 29(8):083602, 2017.

[17] H. Tang, P. Salunkhe, Y.Y. Zheng, J.X. Du, and Y.H. Wu. On the use of synthetic jet actuator arrays for active flow separation control. *Exp. Therm Fluid Sci.*, 57:1–10, 2014.

[18] M. Amitay, D.R. Smith, V. Kibens, D.E. Parekh, and A. Glezer. Aerodynamic flow control over an unconventional airfoil using synthetic jet actuators. *AIAA J.*, 39(3):361–370, 2001.

[19] P. M. Munday and K. Taira. On the lock-on of vortex shedding to oscillatory actuation around a circular cylinder. *Phys. Fluids*, 25(1):013601, 2013. ISSN 1070-6631.

[20] W. Mokhtar, X. Zheng, I. Koc, and K. Kara. Aerodynamics and flow control of flapping wings. In *44th AIAA Aerospace Sciences Meeting and Exhibit*, page 1059, 2006.

[21] M. Çiftci. Synthetic jet application on a flapping airfoil. Master's thesis, Middle east technical university, 2014.

[22] T. Gao and X. Y. Lu. Insect normal hovering flight in ground effect. *Phys. Fluids*, 20(8): 087101, 2008.

[23] P. Lallemand and L.S. Luo. Theory of the lattice boltzmann method: Dispersion, dissipation, isotropy, galilean invariance, and stability. *Phys. Rev. E*, 61(6):6546–6562, 2000.

[24] D. Yu, R. Mei, and W. Shyy. A multi-block lattice boltzmann method for viscous fluid flows. *Int. J. Numer. Methods Fluids*, 39(2):99–120, 2002. ISSN 1097-0363.

[25] P. Lallemand and L. S. Luo. Lattice boltzmann method for moving boundaries. *J. Comput. Phys.*, 184(2):406–421, 2003. ISSN 0021-9991.

[26] C. Wang, H. Tang, S.C.M. Yu, and F. Duan. Active control of vortex-induced vibrations of a circular cylinder using windward-suction-leeward-blowing actuation. *Phys. Fluids*, 28 (5):053601, 2016.

[27] Z. J. Wang. Two dimensional mechanism for insect hovering. *Phys. Rev. Lett.*, 85(10): 2216, 2000.

[28] S. Xu and Z. J. Wang. An immersed interface method for simulating the interaction of a fluid with moving boundaries. *J. Comput. Phys.*, 216(2):454–493, 2006.

[29] S. Izquierdo and N. Fueyo. Characteristic nonreflecting boundary conditions for open boundaries in lattice boltzmann methods. *Phys. Rev. E*, 78(4):046707, 2008.

[30] J. Zhou, R. J. Adrian, S. Balachandar, and T. M. Kendall. Mechanisms for generating coherent packets of hairpin vortices in channel flow. *J. Fluid Mech.*, 387:353–396, 1999. ISSN 1469-7645.